

Coverage Estimation for Secure Ultraviolet Communication

Tao Shan and Julian Cheng

School of Engineering, The University of British Columbia, Kelowna, BC, Canada

Email: tao.shan@ubc.ca, julian.cheng@ubc.ca

Abstract—Existing ultraviolet (UV) channel models for point-to-point communication are unsuitable for estimating the coverage in omni-directional UV communication. To solve this problem, we propose a coverage estimation model based on the Monte-Carlo integration (MCI) method. In this model, we assume that the transmitter is located at the origin, and the receivers pointing to the vertical axis of the origin can be anywhere in a specific area. Meanwhile, we validate the proposed MCI model by comparing it with the Monte-Carlo simulation (MCS) model. The average simulation time of the MCS model can be reduced 30 times by the proposed MCI model. Furthermore, the simulation results demonstrate that the transceiver configurations can affect omni-directional communication coverage. Among all the configuration parameters, the elevation angle of the transmitter is most crucial since it determines the shape of the coverage area significantly. Then we perform the elliptic fitting for the path loss contour and analyze the fitting error. The results show that fitting elliptic can well describe the shape of the coverage, especially the farthest part of the coverage area. This work presents an efficient way to estimate coverage in UV omni-directional communication and provides guidelines for the omni-directional communication system design.

Index Terms—Ultraviolet communication, omni-direction communication, Monte-Carlo Integration, coverage estimation

I. INTRODUCTION

Strong absorption and scattering of ultraviolet (UV) in the atmosphere are the two main features that enable UV communication to realize a non-line-of-sight (NLOS), high security wireless communication within a specific range [1]. These features ensure that UV communication can be used for secure military communication. Both analytical models and stochastic models have been proposed to estimate UV channel performance and communication range. However, most channel models are only applied in point-to-point communication scenarios [2]–[4]. For omni-directional UV communication scenarios, such as secure networking for military groups, there exists few studies that consider the path loss distribution in a specific area and estimate UV NLOS communication coverage. One method to estimate communication coverage is to scan the entire area using a point-to-point single scattering channel model, obtaining the path loss distribution, and perform an elliptic fitting for the path loss contour [5]. Another method is to establish an omni-directional channel model based on the Monte-Carlo simulation (MCS) method [6]. Although these efforts further the study of UV communication technology, easy-to-use and efficient channel models that are

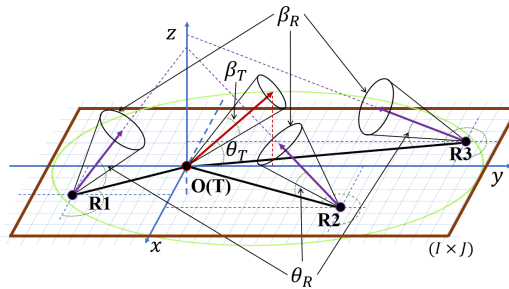


Fig. 1. NLOS omni-directional UV communication geometry

suitable for practical omni-directional scenarios have yet been developed [7].

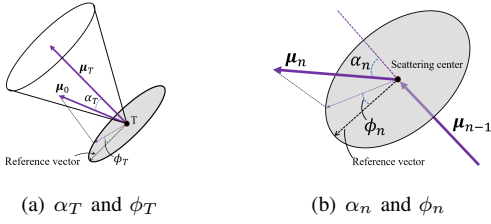
In this paper, we propose a UV communication coverage estimation model based on the Monte Carlo integration (MCI) method. In this model, we assume the transmitter is located at the origin. The receiver points to the vertical axis of the origin and can be located anywhere in the analysis area. We validate the proposed model by comparing it with the existing omni directional MCS model. Furthermore, we analyze the impact of configuration parameters on the communication coverage. Then we perform elliptic fitting for the path loss contour and analyze the fitting error. Compared with the scanning model [5], the proposed model takes both single scattering and multiple scattering into account. Compared with the MCS model [6], the proposed MCI model is more efficient.

II. MONTE-CARLO INTEGRATION MODEL FOR COVERAGE ESTIMATION

Abundant atmospheric scattering of UV photons enables NLOS omni-directional UV communication. Based on the idea of the Monte-Carlo method, we can derive a multiple scattering model to simulate the path loss distribution and estimate the coverage area in omni-directional scenario.

A. Stochastic Model of Multiple Scattering Channel in Omni-directional Scenario

Figure 1 shows a typical geometric setup of the NLOS omni-direction UV communication. The transmitter (T) is fixed at the origin of the Cartesian coordinate system and the direction vector of T is on the $y - z$ plane. The receiver with direction vector pointing to the z -axis is not fixed and can be anywhere on the $x - y$ plane. The elevation angle and the

Fig. 2. α_T and ϕ_T at the transmitter and the α_n and ϕ_n at scattering center

divergence angle of the transmitter are denoted by θ_T and β_T , respectively. The elevation angle and the field-of-view (FOV) angle of the receivers are denoted by θ_R and β_R , respectively. In Fig. 1, without loss of generality, we assume that the area of interest is a rectangle and can be divided into $I \times J$ square sub-areas. If a photon from T can arrive at one sub-area with a non-zero probability $p_{i,j}$, it must go through three processes: emitting from T, propagating and scattering in the media, and arriving at R. If a photon reaches the receiver after the N th scattering, the process of propagating and scattering in the medium will be repeated N times.

Figure 2(a) shows the geometric parameters for photon emitting from the transmitter. The direction cosine of the transmitter is denoted by μ_T . We denote the emitting zenith angle and emitting azimuth angle of by α_T and ϕ_T with respect to μ_T . For a uniform emitted light source, the probability that the propagating direction of the emitted photon is located in an infinitesimal solid angle $d\Omega_T = \sin \theta_T d\theta_T d\phi_T$ is

$$dQ_T = f_{A_T}(\alpha_T) f_{\Phi_T}(\phi_T) d\alpha_T d\phi_T \quad (1)$$

where $f_{A_T}(\alpha_T) = \frac{\cos \alpha_T}{1 - \sin \beta_T}, 0 \leq \alpha_T \leq \frac{\beta_T}{2}$, is the probability density function (PDF) for the emitting zenith angle α_T ; $f_{\Phi(\phi_T)} = \frac{1}{2\pi}, 0 \leq \phi_T \leq 2\pi$ is the PDF for the emitting azimuth angle ϕ_T .

After emitting from the transmitter, the UV photon will propagate and be scattered in the media. The geometric parameters in this process are shown in Fig. 2(b). For an N -order scattering process, we denote the propagating distance to the n th scattering center, the scattering zenith angle and the scattering azimuth angle of the n th scattering, where $n = 1, \dots, N$, by d_n , α_n , and ϕ_n , respectively. The position of the n th scattering center is denoted by $\mathbf{r}_n = [r_{n,x}, r_{n,y}, r_{n,z}]^T$. The direction cosine after the n th scattering is denoted by $\mu_n = [\mu_{n,x}, \mu_{n,y}, \mu_{n,z}]^T$. The scattering zenith angle α_n and the scattering azimuth angle ϕ_n , where $n = 1, \dots, N$, describe the deflection of μ_n with the respect of μ_{n-1} .

For the n th scattering, where $n = 1, \dots, N$, the probability that the propagating direction of the emitted photon is located in an infinitesimal solid angle and the propagating distance in $(d_n, d_n + dd_n)$ is [8]

$$dQ_n = f_D(d_n) f_A(\alpha_n) f_{\Phi}(\phi_n) dd_n d\alpha_n d\phi_n \quad (2)$$

where $f_D(d_n) = k_e e^{-k_e d_n}, 0 \leq d_n \leq \infty$, is the PDF for the propagating distance d_n , and where $k_e = k_s + k_a$ is the extinction coefficient of the transmission medium, and

where k_s and k_a are the scattering coefficient and absorption coefficient, respectively; $f_{\Phi}(\phi_n) = \frac{1}{2\pi}, 0 \leq \phi_i \leq 2\pi$, is the PDF for the scattering azimuth angle ϕ_i ; $f_A(\alpha_n)$, is the PDF for the scattering zenith angle α_n and is determined by the phase function of the scattering process in the transmission medium. For free-space UV communications, $f_A(\alpha_n)$ can be approximated as a normalized and weighted phase function of Rayleigh scattering and Mie scattering [3]

$$f_A(\alpha_n) = \frac{k_s^{Ray}}{k_s} f_A^{Ray}(\alpha_n) + \frac{k_s^{Mie}}{k_s} f_A^{Mie}(\alpha_n), \quad 0 \leq \alpha_n \leq \pi \quad (3)$$

where k_s^{Ray} and k_s^{Mie} are the scattering coefficients for Rayleigh scattering and Mie scattering, respectively, and

$$f_A^{Ray}(\alpha_n) = \frac{3[1 + 3\gamma + (1 - \gamma) \cos^2 \alpha_n]}{8(1 + 2\gamma)} \sin \alpha_n \quad (4)$$

$$f_A^{Mie}(\alpha_n) = \frac{1 - g^2}{2} \left[\frac{1}{(1 + g^2 - 2g \cos \alpha_n)^{\frac{3}{2}}} + f \frac{0.5(3 \cos^2 \alpha_n - 1)}{(1 + g^2)^{\frac{3}{2}}} \right] \sin \alpha_n \quad (5)$$

where the constants γ , g and f are model parameters that can be obtained empirically.

After leaving the last scattering center, i.e., the N -th scattering center, the direction cosine of the UV photon propagation is $\mu_N = [\mu_{N,x}, \mu_{N,y}, \mu_{N,z}]^T$. If the photon moves towards $x - y$ plane (i.e. $\mu_{N,z} < 0$), this photon may reach the $x - y$ plane. The landing position $\mathbf{r}_{N,R}$ can be obtained by

$$\mathbf{r}_{N,R} = \begin{pmatrix} x_{N,R} \\ y_{N,R} \\ 0 \end{pmatrix} = \begin{pmatrix} r_{N,x} + |\frac{r_{N,z}}{\mu_{N,z}}| \mu_{N,x} \\ r_{N,y} + |\frac{r_{N,z}}{\mu_{N,z}}| \mu_{N,y} \\ 0 \end{pmatrix}. \quad (6)$$

We assume that a receiver pointing to the z -axis is at $\mathbf{r}_{N,R}$. If the N -th scattering center is confined within the FOV, we can obtain the detection probability at the subarea (i, j) after N -order scattering

$$p_{R,(i,j)} = H_N I_N \frac{S_r}{l^2 \sin \theta_R} e^{-k_e |\mathbf{r}_{N,R} - \mathbf{r}_N|} \quad (7)$$

where l is the side length of the square sub-area and S_r is the receiving aperture area, (i, j) is the index of sub-area and is determined by the landing position $\mathbf{r}_{N,R}$. H_N and I_N are two indicator functions defined as

$$H_n = \begin{cases} 1, & \text{if the photon moves towards the ground} \\ 0, & \text{otherwise.} \end{cases} \quad (8)$$

and

$$I_n = \begin{cases} 1, & \text{if the } n\text{-th scattering position is in FOV} \\ 0, & \text{otherwise.} \end{cases} \quad (9)$$

Finally, we can obtain the photon receiving probability at sub-area (i, j) after N times scattering as

$$P_{i,j} = \int \int \dots \int_V p_{R,(i,j)} \left(\frac{k_s}{k_e} \right)^N dQ_T dQ_1 \dots dQ_N \quad (10)$$

where V is the whole integration volume with dimension $3N+2$.

B. Monte-Carlo Integration Method and Partial Importance Sampling

Since the closed-form analytical solution for the integral in (10) is theoretically unavailable, we will use a Monte-Carlo integration method to calculate this integral [4].

First, we can rewrite the integral in (10) as

$$P_{i,j} = \int_V g_{N,(i,j)}(\mathbf{d}, \boldsymbol{\theta}, \phi) d\mathbf{d}d\boldsymbol{\theta}d\phi \quad (11)$$

where

$$\begin{aligned} g_{N,(i,j)}(\mathbf{d}, \boldsymbol{\alpha}, \phi) = & p_{R,(i,j)} \left(\frac{k_s}{k_e} \right)^N f_{A_T}(\alpha_T) f_{\Phi}(\phi_T) \\ & \times \prod_{n=1}^N [f_D(d_n) f_{\Theta}(\theta_n) f_{\Phi}(\phi_n)] \end{aligned} \quad (12)$$

and

$$\begin{cases} \mathbf{d} = [d_1, \dots, d_N]^T; \\ \boldsymbol{\alpha} = [\alpha_T, \alpha_1, \dots, \alpha_N]^T; \\ \phi = [\phi_T, \phi_1, \dots, \phi_N]^T; \\ d\mathbf{d}d\boldsymbol{\theta}d\phi = d\alpha_T d\phi_T dd_1 d\alpha_1 d\phi_1 \dots dd_N d\alpha_N d\phi_N. \end{cases} \quad (13)$$

Then, we define an objective function as [4]

$$O_{N,(i,j)}^* = \frac{g_{N,(i,j)}(\mathbf{d}, \boldsymbol{\theta}, \phi)}{f_{N,(i,j)}(\mathbf{d}, \boldsymbol{\theta}, \phi)} \quad (14)$$

where $f_{N,(i,j)}$ is the sampling function, in the integral volume V ($f_N > 0$, $\int_V f_{N,(i,j)} dV = 1$).

Thus, eq. (11) can be rewritten as

$$P_{i,j} = \int_V O_{N,(i,j)}^* f_{N,(i,j)} d\mathbf{d}d\boldsymbol{\theta}d\phi = E[O_{N,(i,j)}^*] \quad (15)$$

where $E[\cdot]$ denotes the mathematical expectation operator. Eq. (15) indicates that if we adopt the sampling function f_N to calculate the mathematical expectation of the objective function O_N^* , the result is equal to receiving probability at the (i,j) -th sub-area, i.e., $P_{i,j}$.

To improve the computation efficiency, we use CPU parallel computing in Matlab and the partial importance sampling [4]. Now the sampling function f_N becomes

$$f_{N,(i,j)} = \prod_{n=1}^N [f_D(d_i) f_{\Phi}(\phi_n)] \prod_{n=1}^N \left[\frac{1}{\pi} \right] \frac{2}{\beta_T} \frac{1}{2\pi}. \quad (16)$$

Then the objective function in (14) becomes

$$O_{N,(i,j)}^* = 2\pi P_{i,j} \left(\frac{k_s}{k_e} \right)^N \frac{\beta_T}{2} \prod_{n=1}^N [f_A(\alpha_n)] \prod_{n=1}^N \pi. \quad (17)$$

Finally, the receiving probability over all the sub-areas can be represented by one two-dimensional matrix \mathbf{P} , which satisfies

$$[\mathbf{P}]_{i,j} = P_{i,j}. \quad (18)$$

Therefore, after all Q sampling points have been simulated, the matrix of path loss within a certain communication region can be obtained by

$$\mathbf{PL} = -10 \log_{10} \left(\frac{\mathbf{P}}{Q} \right). \quad (19)$$

III. SIMULATION RESULTS

We assume that the area is confined to $[-300, 300] \times [-300, 500] \text{ m}^2$ or $[-300, 300] \times [-300, 300] \text{ m}^2$ and the length of the square sub-area $l = 1 \text{ m}$. The number of sample points is $Q = 1 \times 10^9$. The maximum scattering order is three. The remaining model parameters are selected as follows: $(\theta_T, \theta_R, \beta_T, \beta_R) = (45^\circ, 45^\circ, 15^\circ, 60^\circ)$, $Ar = 1.77 \text{ cm}^2$, $\gamma = 0.017$, $g = 0.72$, $f = 0.5$, $(k_a, k_s) = (0.802, 0.550) \text{ km}^{-1}$ at $\lambda = 260 \text{ nm}$ [9]. All the simulations are conducted by Matlab R2021a using a laptop computer with 2.4 GHz CPU and 16 G RAM.

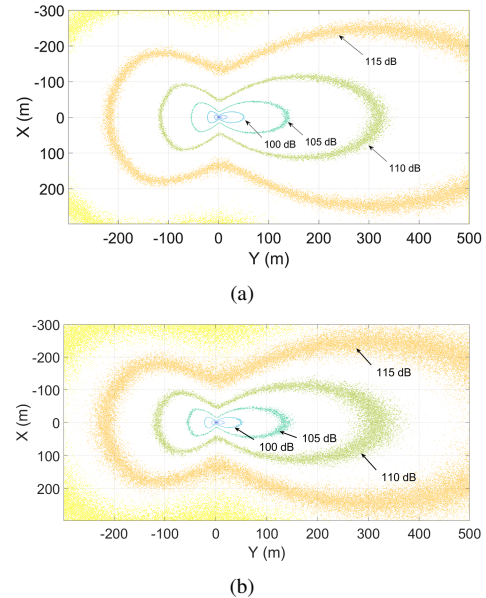


Fig. 3. Path loss contour simulated by different Monte-Carlo models $(\theta_T, \theta_R, \beta_T, \beta_R) = (45^\circ, 45^\circ, 15^\circ, 60^\circ)$: (a) Proposed MCI model; (b) MCS model

Figures 3(a) and 3(b) show the path loss distribution simulated from the proposed MCI model and the MCS model, respectively. Comparing these two results, we can find that the contours and patterns from two different models are the same. Moreover, the average difference and average square difference are 0.1092 dB and 1.4839 dB, respectively. This comparison validates the proposed model. Furthermore, the simulation time of the proposed model is 159.1 seconds if the number of sampling points is 100 million. However, the simulation time of the MCS model [6] with same number of sampling points is 5731.4 seconds. This result indicates that the proposed model is much more efficient than MCS model due to the Monte-Carlo Integration method, the partial importance sampling, and the CPU parallel computing. Furthermore, if we modify the previous MCS model to make it be computed parallelly, the simulation time of the parallel MCS model is 1543.79 seconds, which shows that the proposed MCI model is more efficient.

Figures 4-7 show the relation between the transceiver parameters and the coverage areas. To facilitate our analysis,

we divided the total area into three regions: forward region, backward region, and side region.

First, θ_T significantly determines the shape of the coverage area. As shown in Figs. 4, when the elevation angles of the transmitter θ_T are 10° , 45° , and 90° , the shapes of the coverage area are sharp ellipse, butterfly, and circle, respectively. This is because when θ_T approaches zero, the coverage area only locates in the forward region; while when θ_T approaches 90° , the coverage area becomes uniformly distributed in all regions. Therefore, we conclude that θ_T significantly determines the shape of the coverage area.

Second, β_T mainly determines the area of the side region. Figure 5 shows the path loss contour when the divergence angles of the transmitter β_T are 15° and 60° , respectively. We can see that when β_T increases, the coverage area in the side region increases; while the coverage area in the forward region and the backward region changes slightly. This is because when β_T approaches zero, the light beam concentrate on one point, then the probability of the photon leaks to the side region also approaches zero; when β_T is large, the light beam is divergent enough such that the probability of the photon leaks to the side region increases greatly. Therefore, we conclude that β_T mainly determines the area of the side region.

Third, θ_R mainly adjusts the area of the backward region. Figures 6 are the path loss contour when the elevation angles of the receiver θ_R are 30° , 60° , respectively. We can see that when θ_R increases, the coverage area in the backward region shrinks. This is because when θ_R is small, the FOV area can have a common volume with the beam if the receiver locates in the backward region; while when θ_R is large, the common volume vanishes if the receiver locates in the backward region. Therefore, we conclude that θ_R mainly adjusts the area in the backward region.

Fourth, β_R mainly adjusts the area of all regions. Fig. 7 shows the coverage areas when the FOV angles of the receiver β_R are 30° and 60° , respectively. We can see that when β_R increases, the areas of all regions increases. This is because the increase of the FOV angle can always increase the probability of detecting a photon at the receiver. Therefore, we conclude that β_R mainly adjusts the area of all regions.

IV. CURVE FITTING OF THE COVERAGE FOR DIFFERENT PATH LOSS

All the contours obtained from the MCI model are based on simulation. However, in certain applications, such as coverage customization, it is important to describe the desired coverage area analytically. This requires us to fit the coverage areas under different transceiver parameters to some shapes with analytical expression.

As mentioned in previous Section, the shape of the coverage area is mainly determined by the elevation angle of the transmitter θ_T , and there are three types of coverage shape: the ellipse, the butterfly, and the circle. However, if we regard the butterfly as a combination of two ellipses and regard the circle as a special case of a ellipse, we can always use the ellipse

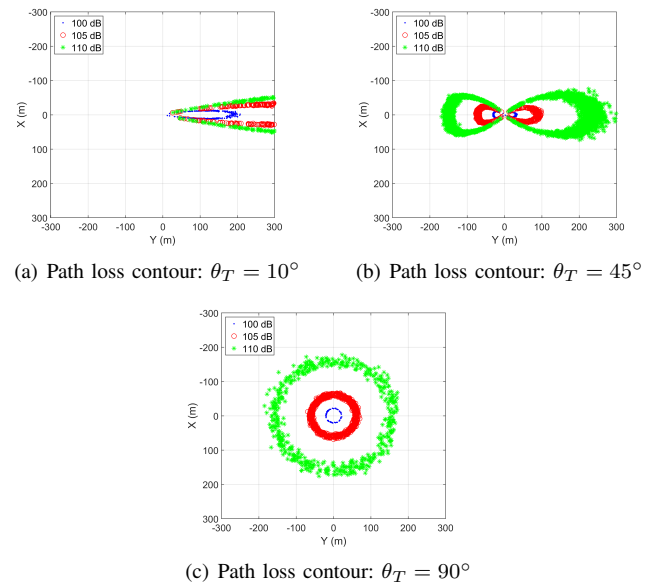


Fig. 4. Path loss contour ($\beta_T = 15^\circ$, $\theta_R = 30^\circ$, $\beta_R = 30^\circ$)

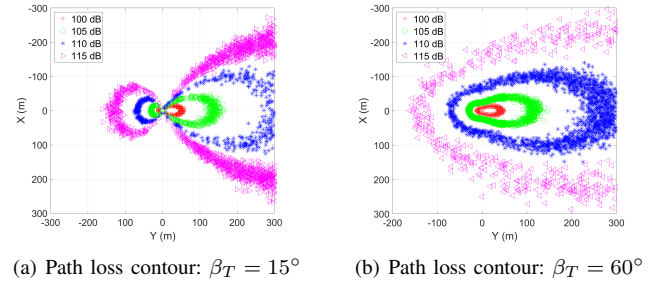


Fig. 5. Path loss contour ($\theta_T = 45^\circ$, $\theta_R = 60^\circ$, $\beta_R = 60^\circ$)

to fit the coverage area when the required fitting precision is not high. Therefore, in the following, we use the ellipse to fit all the coverage areas.

Besides, if we consider the practical implementations, the scenarios can be divided into two types:

- (1) the legitimate users are distributed in a wide area;
- (2) the legitimate users are concentrated in a small area.

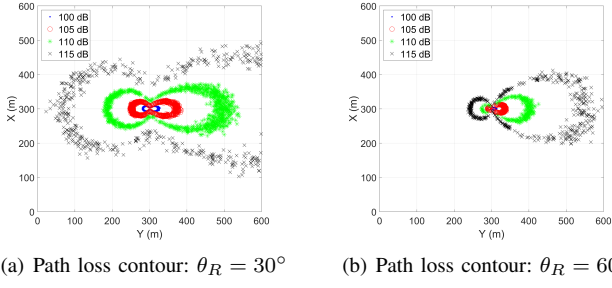
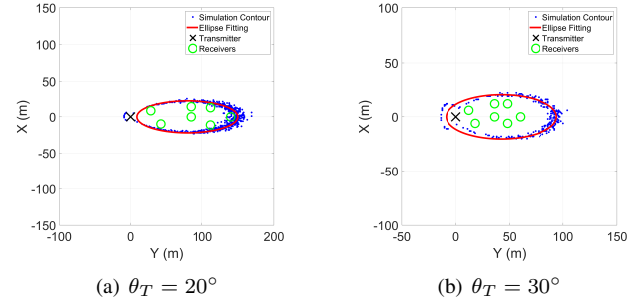
In the first scenario, the only solution to cover all the legitimate users is to use a large elevation angle of the transmitter θ_R and a large divergence beam angle β_T . Therefore, the second scenario is a more complicated but meaningful case. In the following, we only consider the second scenario, where all the legitimate users are concentrated in a small area.

We perform the fitting based on the following elliptic function

$$\frac{(x - x_0)^2}{b^2} + \frac{(y - y_0)^2}{a^2} = 1 \quad (20)$$

where $x_0 = 0$ because the direction vector of transmitter is on the $y - z$ plane. The fitting ellipse parameters y_0 , a , b can be calculated based on the least squares criterion

$$\min_{y_0, a, b} \sum_{i=1}^M \left[a^2 \left(1 - \frac{y_0^2}{b^2} + \frac{2y_0}{b^2} y_i - \frac{y_i^2}{b^2} \right) - x_i^2 \right]^2 \quad (21)$$

(a) Path loss contour: $\theta_R = 30^\circ$ (b) Path loss contour: $\theta_R = 60^\circ$ Fig. 6. Path loss contour ($\theta_T = 45^\circ$, $\beta_T = 60^\circ$, $\beta_R = 30^\circ$).(a) Path loss contour: $\beta_R = 30^\circ$ (b) Path loss contour: $\beta_R = 60^\circ$ Fig. 7. Path loss contour ($\theta_T = 45^\circ$, $\beta_T = 60^\circ$, $\theta_R = 90^\circ$)

where M is the number of points.

After obtaining y_0 , a , b , one can plot the fitting ellipse.

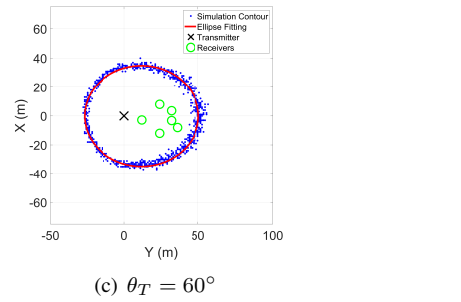
Figure 8(a) shows the coverage areas and the corresponding fitting ellipses when the transmitter elevation angle $\theta_T = 20^\circ$. When the transmitter elevation angle is small, the coverage and the corresponding ellipse are long and narrow, i.e., the short axis of the ellipse is much smaller than the long axis. Although error exists near the transmitter, the fitting ellipse well describes the shape of the coverage, especially the farthest part of the coverage area.

Figure 8(b) shows the coverage areas and the corresponding fitting ellipses when the transmitter elevation angle $\theta_T = 30^\circ$. In this condition, the contour is no longer narrow and spans from the backward region to the forward region. Similar to the low elevation condition, the ellipse curve can well model the most part of the contour, especially the farthest part of the contour. The main fitting error exists in the backward region and the side regions near the transmitter. The elliptical curve fitting underestimates coverage area in the backward region and overestimates coverage area in the side regions.

Figure 8(c) show the contours and the corresponding fitting ellipses when the transmitter elevation angle $\theta_T = 60^\circ$. Compared with low θ_T condition and middle θ_T condition, the high θ_T condition produces the most regular closed curve. Thus, the fitting error is the smallest.

V. CONCLUSION

We proposed a Monte-Carlo integration model for estimating coverage in the UV omni-directional communication scenario. The proposed model can reduce the average simulation time of the MCS model by 30 times. Furthermore, we analyzed the impact of transceiver configurations on the shape

Fig. 8. Contour and corresponding fitting ellipse ($\beta_T = 25^\circ$, $\theta_R = 50^\circ$, $\beta_R = 90^\circ$)

of coverage area. The simulation results indicated that the coverage area could be altered by adjusting the configuration parameters. Then, an ellipse was used to fit the path loss contour. The fitting results show that the coverage area can be well described by an ellipse with an analytical expression. This easy-to-use expression helps map the parameters of the specific coverage shape to the parameters of transceiver configurations, which helps customize the coverage of secure wireless networks.

REFERENCES

- [1] R. Yuan and J. Ma, "Review of ultraviolet non-line-of-sight communication," *China Communications*, vol. 13, no. 6, pp. 63–75, 2016.
- [2] M. R. Luetgen, D. M. Reilly, and J. H. Shapiro, "Non-line-of-sight single-scatter propagation model," *J. Opt. Soc. Am. A*, vol. 8, no. 12, pp. 1964–1972, Dec. 1991.
- [3] H. Ding, G. Chen, A. K. Majumdar, B. M. Sadler, and Z. Xu, "Modeling of non-line-of-sight ultraviolet scattering channels for communication," *IEEE J. Sel. Areas Commun.*, vol. 27, no. 9, pp. 1535–1544, Dec. 2009.
- [4] R. Yuan, J. Ma, P. Su, Y. Dong, and J. Cheng, "Monte-carlo integration models for multiple scattering based optical wireless communication," *IEEE Trans. Commun.*, vol. 68, no. 1, pp. 334–348, Nov. 2019.
- [5] H. Qi, D. Zou, C. Gong, and Z. Xu, "Two-dimensional intensity distribution and adaptive power allocation for ultraviolet ad-hoc network," *IEEE Trans. Green Commun. Netw.*, vol. 6, no. 1, pp. 558–570, March. 2022.
- [6] T. Shan, J. Ma, T. Wu, Z. Shen, and P. Su, "Modeling of ultraviolet omnidirectional multiple scattering channel based on monte carlo method," *Opt. Lett.*, vol. 45, no. 20, pp. 5724–5727, Oct. 2020.
- [7] Z. Ghassemlooy, S. Arnon, M. Uysal, Z. Xu, and J. Cheng, "Emerging optical wireless communications—advances and challenges," *IEEE J. Sel. Areas Commun.*, vol. 33, no. 9, pp. 1738–1749, Sept. 2015.
- [8] H. Ding, Z. Xu, and B. M. Sadler, "A path loss model for non-line-of-sight ultraviolet multiple scattering channels," *EURASIP J. Wirel. Commun. Netw.*, vol. 2010, pp. 1–12, Dec. 2010.
- [9] R. J. Drost, T. J. Moore, and B. M. Sadler, "Uv communications channel modeling incorporating multiple scattering interactions," *J. Opt. Soc. Am. A*, vol. 28, no. 4, pp. 686–695, Apr. 2011.